Graphene-Carbon Nanotube Hybrids as Robust Catalyst Supports in Proton Exchange Membrane Fuel Cells

Kien-Cuong Pham,[a,b] David S. McPhail,[b] Cecilia Mattevi,[b] Andrew T. S. Wee,[a,c] and Daniel H. C. Chua[d,z]

[a]*NUS Graduate School for Integrative Sciences and Engineering (NGS), National University of Singapore, Singapore 117456, Singapore*
[b]*Department of Materials, Imperial College London, London, SW7 2AZ, United Kingdom*
[c]*Department of Physics, National University of Singapore, Singapore 117542, Singapore*
[d]*Department of Materials Science and Engineering, National University of Singapore, Singapore 117576, Singapore*

Catalyst degradation is one major challenge preventing the worldwide commercialization of the Proton Exchange Membrane Fuel Cells. In this study, we investigate the development of a novel hierarchical carbonaceous support for the platinum catalysts, called graphene-carbon nanotube hybrids (GCNT), and its degradation behavior during an accelerated degradation test. The carbon support is fabricated by growing graphene directly onto carbon nanotubes to form a unique all-carbon nanostructure possessing both an ultra-high density of exposed graphitic edges of graphene and a porous structure of carbon nanotubes. The GCNT-supported platinum catalyst exhibits a higher intrinsic catalytic activity than a carbon black-supported platinum catalyst, and much higher than a CNT-supported platinum catalyst. The enhanced catalytic activity of the GCNT-supported platinum catalyst is explained by the high graphitic edge density which promotes the catalytic reactions on platinum catalyst. The GCNT-supported platinum catalyst also exhibits a superior electrochemical stability over that of the carbon black-supported platinum catalyst, explained by the high crystallinity of the GCNT support. The superior stability is expressed by a lower loss in polarization performance, a smaller increase in charge transfer resistance, a lower loss in the platinum electrochemical surface area, a lower rate of carbon corrosion, and a more stable catalyst microstructure.

Manuscript submitted November 12, 2015; revised manuscript received December 21, 2015. Published January 7, 2016.

Energy security and climate change have become major global concerns, and viable candidates for renewable energy technologies are actively being sought. With high energy conversion efficiencies and low emissions, fuel cell technologies have received much research attention recently.[1,2] Among the different fuel cell technologies, the Proton Exchange Membrane Fuel Cells (PEMFCs) have been identified as the most suitable candidate for transportation and portable applications.[1,3] The PEMFCs possess high power density, low working temperature, quick start-up and quiet operation.[1,4,5] In spite of their great potential, PEMFCs have not been widely commercialized. One major challenge of the PEMFC technology is the unsatisfactory durability of the device.[6–8] Enhancing device durability is essential for the commercialization of PEMFCs.

The performance of PEMFCs often degrades slowly during their lifetime. The performance degradation is believed to be caused by at least several phenomena, including Pt catalyst aggregation/coalescence, Pt dissolution (and re-deposition inside the membrane), and Pt detachment due to the corrosion of carbonaceous supports.[9,10] Pt catalyst aggregation/coalescence happens when Pt catalyst is dissolved in the form of soluble ions (such as Pt^{2+}) at high potentials and then re-deposited on nearby Pt catalyst nanoparticles.[8,9] The aggregation/coalescence process results in a decrease of the active Pt electrochemical surface area, and therefore a degradation of the device performance. Pt re-deposition in Nafion membrane happens when platinum ions diffuse into the membrane and re-deposit as isolated Pt nanoparticles.[9,11–13] These isolated Pt nanoparticles are not active in electrochemical reactions and result in a loss of electrode activity. Pt loss can also happen in the form of Pt catalyst detachment caused by the corrosion of carbonaceous supports.[14,15] Presently, the most popular electrocatalysts in PEMFC electrodes are Pt nanoparticles deposited on carbon black materials, such as Vulcan XC72 (VXC72).[2,16] However, carbon black materials are susceptible to corrosion under PEMFC working conditions (high water content, high potential, low pH and elevated temperature) due to their low crystallinity, exacerbated by the presence of platinum catalyst.[17] A good carbon support for electrocatalysts in PEMFC electrodes should have good electrical conductivity and high degree of crystallinity.[16] Graphitic nanomaterials including carbon nanotubes (CNTs) and graphene, with their extraordinary electrical and mechanical properties as well as high degrees of crystallinity, could offer more advanced alternatives.

Recently, CNTs have been employed as alternative catalyst supports in PEMFCs with promising electrochemical durability.[14,18,19] However, in order to achieve a higher dispersion of Pt nanoparticles, the inert graphitic basal plane surface of CNTs generally requires functionalization, which may significantly reduce their electrical conductivity.[20] In contrast to CNTs, graphene can offer edge plane anchor sites for the Pt catalyst nanoparticles. Furthermore, it has been suggested that the heterogeneity of carbon support with edge planes can better stabilize and enhance the catalytic activity of the Pt catalyst.[20] However, the two-dimensional morphology of graphene can impede the transport of reactants inside the fuel cells, due to the tendency to re-stack graphene unless the graphene is suitably aligned. To address this challenge, we reported in our previous study[21] the growth of a hierarchical carbon nanostructure in which CNTs are grown directly onto Toray carbon paper and graphene is directly and densely grown onto the CNTs. We refer to this material as graphene-carbon nanotube (GCNT) hybrids. The GCNT hybrids possess an ultra-high density of exposed graphene edges while retaining the porous structure of CNTs on carbon paper, suitable for an advanced catalyst support in PEMFCs. The magnetron sputtering electrocatalyst preparation method is used to deposit an ultra-low loading of Pt onto the GCNT hybrids to fabricate an integrated, polytetrafluoroethylene binder-free cathode for PEMFCs. Following this approach, our previous study showed that graphene-carbon nanotube hybrids demonstrated an enhanced polarization performance compared to a commercial carbon black-supported Pt catalyst.[21] Device durability, nevertheless, was not discussed in our previous report. In this study, we will focus on the electrochemical durability of the catalyst based on the graphene-carbon nanotube hybrid support.

In this study, the durability of GCNT-supported Pt catalyst is compared to a commercial carbon black-supported and a CNT-supported Pt catalysts through an accelerated degradation test. The degradation

[z]E-mail: msechcd@nus.edu.sg

of the materials is investigated from several perspectives, including: (1) total device polarization performance losses, with deconvolution of the electrochemical processes using electrochemical impedance spectroscopy; (2) evidences of Pt catalyst electrochemical surface area loss and carbon corrosion from cyclic voltammetry measurements; and (3) electrode structural study using transmission electron microscopy technique.

Experimental

Growth of the graphene-carbon nanotube hybrids.—The GCNT hybrids were grown on carbon paper to form an integrated, binder-free, high surface area and conductive electrode as reported elsewhere.[21] To summarize, the GCNT hybrids were grown directly onto Toray carbon paper using a two-step procedure. In the first step, CNTs were grown directly onto the catalyzed carbon paper using the thermal chemical vapor deposition technique. In the second step, graphene was grown directly onto the CNTs without any additional catalyst, using the radio frequency plasma enhanced chemical vapor deposition technique.

Electrodes and membrane electrode assembly fabrication.—A detailed description of the electrodes and membrane electrode assembly fabrication method was reported in our previous study.[21] To summarize, the GCNT hybrids were used to fabricate the Pt-deposited cathode (Pt/GCNT) for electrochemical evaluation. The GCNT hybrids were deposited with platinum (19 nm nominal thickness, equivalent to an ultra-low Pt loading of 0.04 mg cm^{-2}) using the magnetron sputtering technique.

For comparison purposes, two reference cathodes were prepared. The first reference cathode was fabricated using a commercial carbon black-supported Pt catalyst (Pt/VXC72, Premetek), with a Pt loading of 0.04 mg cm^{-2} using the conventional catalyst-ink method. The second reference cathode was fabricated by sputtering Pt onto the CNTs on carbon paper (Pt/CNT) with a Pt loading of 0.04 mg cm^{-2}.

To prepare the membrane electrode assembly (MEA), standard anodes were fabricated with the commercial catalyst Pt/VXC72 (Premetek) at a high Pt loading of 0.2 mg cm^{-2} using the conventional catalyst-ink method. All MEAs were prepared with Nafion 212 (DuPont) as the proton exchange membrane. Cathodes of interest, Nafion proton exchange membrane, and standard anodes were bonded together to form MEAs using a hot-press method.

Electrochemical evaluations.—The polarization measurements were carried out in a single cell test station (5 cm^2, Electrochem. Inc. 890B) at 80°C under fully humidified H_2 (99.999%) and O_2 (99.7%). H_2 and O_2 were pressurized at 30 psi with base flow rates of 300 sccm and stoichiometric flow rates of 14 sccm A^{-1} and 7 sccm A^{-1}, respectively.

Electrochemical impedance spectroscopy (EIS) was performed under the same conditions as the polarization measurements, using an Autolab potentiostat (PGSTAT302N, Metrohm) equipped with a frequency response analyzer (FRA2.V10). EIS was performed at cell potentials of 0.7 V, 0.6 V and 0.5 V, with an AC perturbation amplitude of 40 mV and in a frequency range between 10 kHz and 0.01 Hz.

To assess the electrochemical stability of the cathodes, in situ accelerated degradation tests (ADTs) were performed using the aforementioned Autolab potentiostat. While conducting ADT, O_2 in the cathode compartment was replaced by N_2. N_2 and H_2 flow rates were 30 sccm and 50 sccm, respectively, under ambient pressure. ADT was performed by a rectangular-waveform oxidative potential cycling of the cathode (working electrode) between 0.6 V (for 40 s) and 1.4 V (for 20 s) vs. hydrogen anode per cycle, for 100 cycles. The anode served as both a counter electrode and a reversible hydrogen electrode (RHE). Cyclic Voltammetry (CV) measurements were performed before ADT and after every 10 oxidative cycles. The CV measurements were carried out between 0.05 V and 1.2 V vs. RHE, at a scan rate of 50 mV s^{-1} using the aforementioned Autolab potentiostat fitted with a SCANGEN analogue scan generator.

Finally, after ADT, polarization and EIS measurements were performed again to assess the post-ADT performance of the MEAs.

Physical characterization.—The morphology of the GCNT and Pt/GCNT electrodes was characterized with field emission scanning electron microscopy (FE-SEM, JEOL JSM-6700F). The chemical state analysis of the Pt/GCNT electrode was obtained using X-ray Photoelectron Spectroscopy (XPS) (Omicron 7-channeltron analyzer) with Mg K_α X-ray source (1253.6 eV photon energy, Omicron X-ray twin anode source). Constant analyzer energy (CAE) modes of 50 eV and 20 eV were used for survey scan and high resolution scans, respectively. The electrode structural study was performed with transmission electron microscopy (TEM, JEOL JEM-2010F). Cross-sectional TEM lamellae of the assembled MEAs with Pt/GCNT and Pt/VXC72 cathodes, both before and after the degradation test, were prepared for TEM examinations. A Scanning Electron Microscopy-Focused Ion Beam sample preparation technique (SEM-FIB dual beam, FEI Helios NanoLab 600) was used to prepare the TEM lamellae specifically selected from the interface region between the studied cathodes and the Nafion membrane. The FIB sample preparation technique is much less destructive to the MEA structure than other TEM sample preparation techniques such as ultramicrotomy technique where damages to the sample structure and Pt nanoparticles smearing/cross-contamination are hard to avoid. TEM lamellae prepared by FIB method, therefore, reflect more faithfully the microstructure of the MEAs and their changes caused by the accelerated degradation test.

Results and Discussion

Physical characterization.—The morphological characterization of the GCNT and Pt/GCNT electrodes was obtained with FE-SEM and is shown in Figs. 1a–1b. Fig. 1a shows the SEM micrograph of the GCNT hybrids. The hybrids possess a unique nanostructure featuring a fibrous morphology associated with the characteristics of CNTs, and leaf-like graphene grafted directly on and along the CNTs at an ultra-high density. The hybrids are uniform in size and morphology, with an average overall diameter of approximately 100 nm. The hybrids were grown densely and uniformly while retaining good porosity. These characteristics are highly valuable for the PEMFC electrode applications, offering a high surface area catalyst support while ensuring efficient mass transport and good catalyst accessibility. It is clear that the hybrids offer a high density of exposed edges, which is not possible for ordinary CNTs where inert basal graphitic planes are exposed instead. When the hybrids are used as catalyst supports for Pt in a fuel cell electrode, the high density of graphene edges offers numerous anchor points for the Pt catalyst nanoparticles. Fig. 1b shows the SEM micrograph of the Pt/GCNT hybrids. The SEM micrograph shows that the Pt/GCNT retains the overall structure of the GCNT hybrids, with a thickening of the leaf-like features due to the deposition of Pt. For a better understanding of the GCNT and Pt/GCNT hybrids, interested readers can find a comprehensive characterization of the GCNT and Pt/GCNT hybrid materials, including SEM, TEM, Raman spectroscopy and X-ray photoelectron spectroscopy (XPS), in our previous report.[21]

The purity and chemical state of the Pt/GCNT catalyst were characterized with XPS. Fig. 1c shows the survey scan XPS wide spectrum of the Pt/GCNT catalyst. The spectrum is dominated by a set of characteristic peaks of Pt, most dominantly the Pt 4f peaks. The two additional elements identified are oxygen and carbon, as evidenced by O 1s peak in the 525–535 eV binding energy region and C 1s peak in the 280–290 eV binding energy region. The presence of both elements are expectable, due to the air exposure and the signal contribution from the carbon-based GCNT support. The Pt 4f high resolution scan is presented in Fig. 1d. After subtracting a Shirley background, the Pt 4f XPS spectrum is fitted using three Gaussian-Lorentzian "f" doublets with a spin-orbit splitting of 3.3 eV. The three doublets are identified by the position of the Pt $4f_{7/2}$ peak at binding energies of 71.1 eV, 72.4 eV and 74.0 eV, attributed to the elemental state Pt^0, oxidized states Pt^{2+} and Pt^{4+}, respectively.[22] The binding energies are referenced to

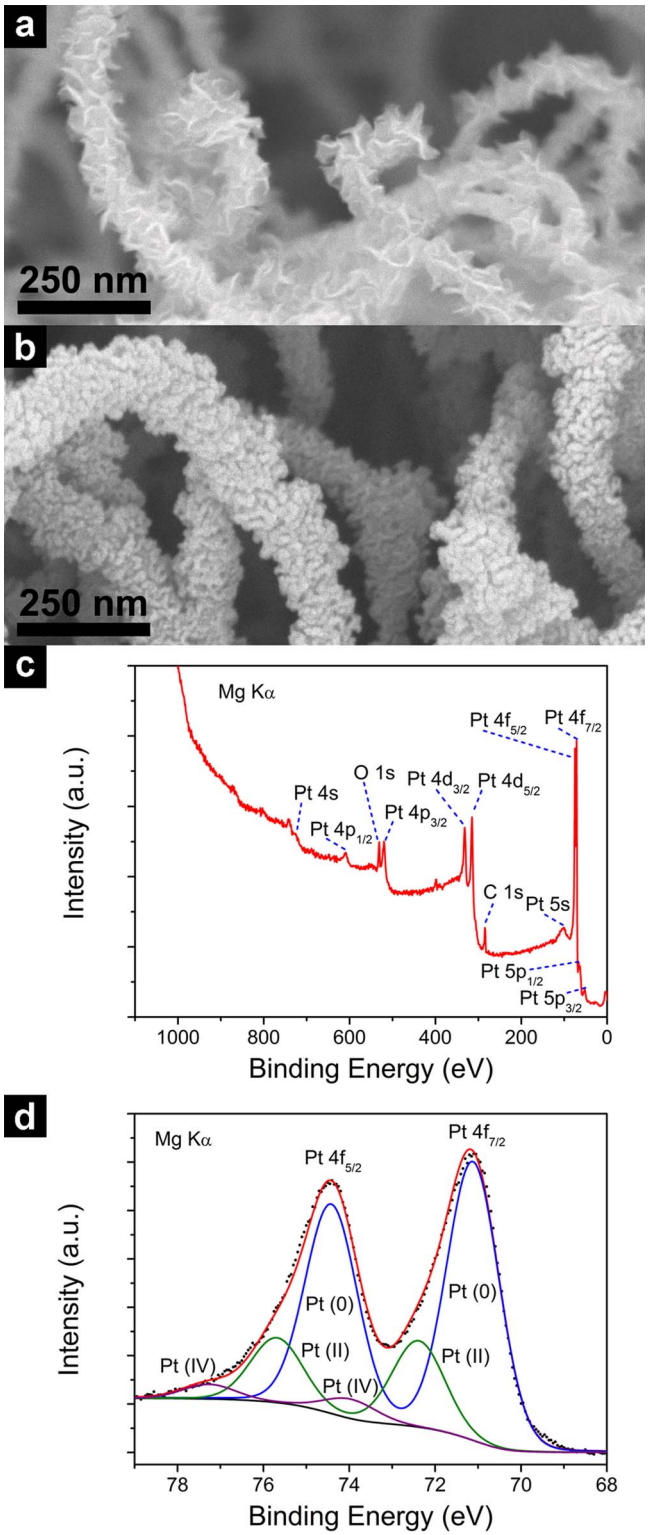

Figure 1. Physical characterization of the GCNT and Pt/GCNT hybrids. Morphological characterization with FE-SEM of (a) the GCNT hybrids and (b) the Pt/GCNT hybrids. XPS characterization of the Pt/GCNT hybrids with (c) XPS survey spectrum and (d) Pt 4f high resolution scan.

the C 1s binding energy of 284.44 eV. The respective concentrations of the three chemical states are 72.5%, 22.4% and 5.1%. The surface oxidation of Pt upon exposure to the air is expectable, as oxygen is readily chemisorbed onto the surface of Pt nanoparticles, especially at the kink and step sites of the nanocrystals.[22] The elemental state

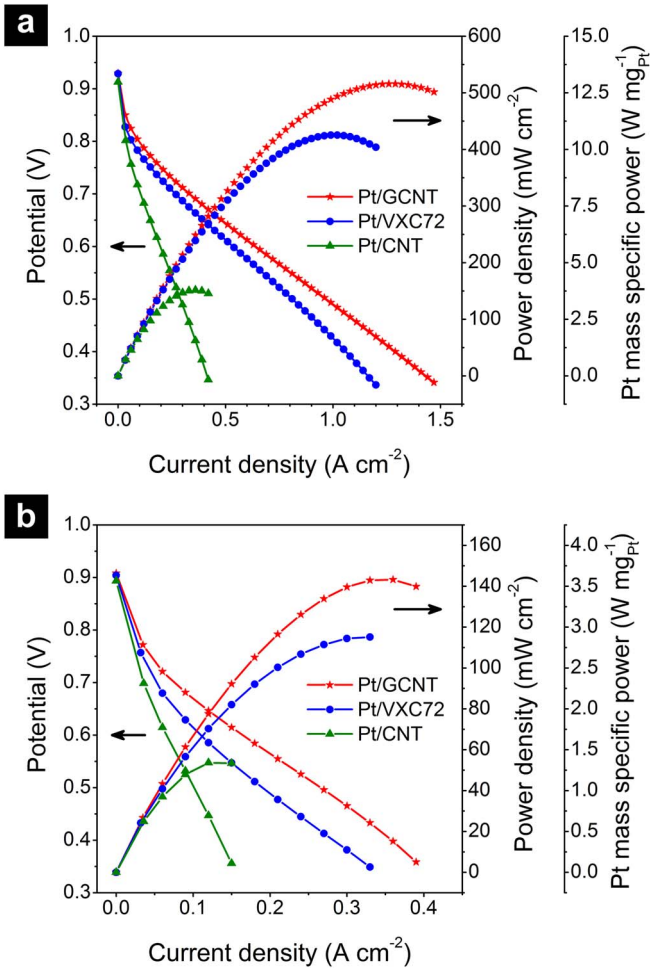

Figure 2. Polarization curves of the Pt/GCNT, Pt/VXC72 and Pt/CNT cathodes (a) before and (b) after the accelerated degradation test.

Pt^0 $4f_{7/2}$ binding energy is found to be in good agreement with the reported literature, with no significant energy shifts identified. Tang et al. reported a Pt^0 $4f_{7/2}$ binding energy of 71.1 eV as referenced to the C 1s binding energy of 284.4 eV, for the magnetron sputtered Pt-on-CNT catalyst.[14] Lewera et al. reported a Pt^0 $4f_{7/2}$ binding energy of 71.19 eV as referenced to the C 1s binding energy of 284.44 eV, for a commercial Pt/carbon black catalyst.[23] The elemental state Pt^0 $4f_{7/2}$ binding energy of bulk Pt is 71.2 eV.[24]

The degradation of device performance from a polarization perspective.—The performance of the Pt/GCNT cathode was first assessed for the total device polarization. The Pt/GCNT, Pt/VXC72 and Pt/CNT cathodes were tested for polarization performance. The three cathodes have the same Pt loading of 0.04 mg cm^{-2}. Fig. 2a shows the polarization curves for the fresh Pt/GCNT, Pt/VXC72 and Pt/CNT cathodes. The Pt/GCNT cathode demonstrates a remarkably improved polarization performance over both commercial Pt/VXC72 and Pt/CNT cathodes throughout the current density range. The maximum power densities per cathode Pt loading of Pt/GCNT, Pt/VXC72 and Pt/CNT cathodes are 12.9, 10.6 and 3.79 W mg^{-1}_{Pt}, respectively. The maximum power density of the Pt/GCNT cathode is 21% and 240% higher than those of the Pt/VXC72 and Pt/CNT cathodes, respectively. Another benchmark for the comparison of polarization curves is the power density obtained at 0.6 V.[25] Similarly, the Pt-mass specific power densities at 0.6 V of the Pt/GCNT, Pt/VXC72 and Pt/CNT cathodes are 9.58, 8.05 and 2.94 W mg^{-1}_{Pt}, respectively. The power density at 0.6 V of the Pt/GCNT cathode is 19% and 226% higher than those of the Pt/VXC72 and Pt/CNT cathodes. By

both measures, the Pt/GCNT cathode shows approximately a 20% improvement in power densities over the Pt/VXC72 cathode and a great improvement over the Pt/CNT cathode.

In order to examine the electrochemical stability of the Pt/GCNT cathode in comparison with the Pt/VXC72 and Pt/CNT cathodes, all cathodes underwent the accelerated degradation test (ADT), as elaborated in the Experimental section. The dynamic oxidative potential cycling in ADT was used to mimic the real working conditions of PEMFCs.[14] The lower potential of 0.6 V vs. RHE simulates the normal working state of PEMFCs. The upper potential of 1.4 V vs. RHE simulates the fuel cell start-up/shut-down events. High cathode potentials during such events accelerate the Pt loss and carbon corrosion in the cathode and result in severe degradation of PEMFC performance.[26] After the ADT, the polarization performance were compared again, as shown in Fig. 2b. The Pt/GCNT cathode once again demonstrates a superior power output to the Pt/VXC72 and Pt/CNT cathodes in the entire range of the polarization curve. The maximum power density and the power density at 0.6 V of the Pt/GCNT cathode are 24% and 49% higher than those of the Pt/VXC72 cathode, up from the 21% and 19% enhancements demonstrated in the fresh electrodes. The results suggest a much better electrochemical stability in the Pt/GCNT cathode compared to the Pt/VXC72 cathode from the polarization curve perspective.

Deconvolution of polarization losses using electrochemical impedance spectroscopy.—Whilst the Pt/GCNT cathode shows remarkable enhancements in polarization performance and durability from the polarization perspective compared to the Pt/VXC72 cathode, the polarization performance of an electrode depends on several processes, including electrode reaction kinetics, ohmic loss and mass transfer. In order to compare the electrode reaction kinetics and its changes after the degradation test, a deconvolution of the polarization losses using electrochemical impedance spectroscopy is required.

For a deconvolution of polarization losses present in studied cathodes, electrochemical impedance spectroscopy measurements were performed at a series of cell potentials of 0.7 V, 0.6 V and 0.5 V for the Pt/GCNT, Pt/VXC72 and Pt/CNT cathodes, both before and after the degradation test. Fig. 3 shows the EIS plots of the studied electrodes at various cell potentials, as well as the equivalent circuit fittings of the data. Figs. 3a and 3b show the Nyquist plot and Bode plots of the EIS measurement for the Pt/GCNT electrode before ADT, performed at a cell potential of 0.6 V which is considered a regular working potential of PEMFCs. The EIS plots in Figs. 3a and 3b are representative for other electrodes and at other cell potentials. The equivalent circuit fitting is performed using the circuit presented in Fig. 3c.

In Fig. 3a, the Nyquist plot shows following features. Firstly, it is noted that at high frequency range, the plot shows an inductive response. This is commonly seen in electrochemical systems with very low impedances such as fuel cells. The high frequency inductive response is explained by the parasitic inductance present in the instrument and cables (represented by a L_{cab} element in Fig. 3c). The presence of this high frequency inductance necessitates a proper equivalent circuit fitting to determine the ohmic resistance present in the system. With the presence of the high frequency inductance element, the first intersection point at high frequency between the Nyquist plot and the real impedance axis Z' may slightly deviate from the ohmic resistance value.[27] The ohmic resistance present in the system, including membrane, electrodes and contact resistances, is represented by a R_{ohm} element in Fig. 3c. Secondly, the main capacitive arc of the EIS plot is considered a compound arc formed from at least two constituent arcs. As it will become clear later, the first constituent arc present at high frequency range is independent of the cell potentials, and is therefore attributed to non-faradaic origins, such as distributed ionic resistance/double layer charging within the porous catalyst layer or electrical contact resistance/contact capacitance.[28] This arc is represented by a non-faradaic resistance R_{nF} in parallel with a capacitive constant phase element $CPE_{nF\text{-}c}$. The second constituent arc present at medium and low frequency range is potential-dependent, and is therefore attributed to electrochemical reaction kinetics and mass transfer process. The impedance is represented by a charge transfer resistance (R_{ct}, representing the electrochemical reaction kinetics), a bounded Warburg impedance (O, representing the finite mass transfer process), and a capacitive constant phase element ($CPE_{dl\text{-}c}$, representing the double layer capacitance of electrode). Thirdly, it is noted that the Nyquist plot exhibits two inductive loops present at low frequency range. This low frequency inductive response was also reported in some other studies.[28–32] In contrast to the high frequency inductance, the low frequency inductance is considered part of the real electrochemical processes happening in the system.[29] The low frequency inductance is suggested to originate from Pt oxidation[29] or additional relaxation processes involving the adsorption of reaction intermediates in the oxygen reduction reaction.[28,29] The inductive response is observed in our experiments at various cell potentials, including a lower cell potential of 0.5 V. The Pt oxidation is not likely at this low cell potential. The adsorption of reaction intermediates are, therefore, more likely to be the cause of this inductive response. The two inductive loops are represented by two resistance elements $R_{ad\text{-}1}$ and $R_{ad\text{-}2}$ as well as two corresponding inductive constant phase elements $CPE_{ad\text{-}i\text{-}1}$ and $CPE_{ad\text{-}i\text{-}2}$. These two inductive loops may be attributed to two relaxation processes of adsorbed reaction intermediates during the oxygen reduction reaction on Pt nanoparticles.[28] We note that, with the presence of the inductive loops at low frequency, the intersection of the Nyquist plot with the real impedance axis Z' at low frequency can significantly deviate from the steady state total impedance of the electrochemical system. A similar observation was also reported by Roy et al.[29] As a simplified model of PEMFCs, a simple Randle circuit is commonly used to fit the EIS data. However, we strongly suggest that the low frequency inductive response, if present, cannot be ignored. In such case, a simple Randle circuit fitting is unrealistic and can result in significant errors in the determination of electrode parameters. A more appropriate model such as in Fig. 3c is required. Mathematical expressions of the circuit elements used in our circuit fitting are presented in Table I. Figs. 3d–3f show the Nyquist plots and the equivalent circuit fitting curves of the Pt/GCNT, Pt/VXC72 and Pt/CNT electrodes before ADT at various cell potentials. All equivalent circuit fittings use the circuit presented in Fig. 3c.

To compare the durability of electrodes, EIS measurements of the Pt/GCNT, Pt/VXC72 and Pt/CNT electrodes are contrasted between their respective before-ADT and after-ADT states. Fig. 4 shows the EIS measurements at 0.6 V of the studied electrodes both before ADT and after ADT. Qualitatively, the Pt/GCNT electrode clearly shows a smaller relative broadening of the EIS curve than that of the Pt/VXC72 electrode, which suggests a better stability demonstrated by the Pt/GCNT electrode. Whilst the Pt/CNT electrode shows the smallest relative broadening of the EIS curve, its EIS curves are always broader than those of the Pt/GCNT and Pt/VXC72 electrodes, which suggests a low catalytic activity of the Pt/CNT electrode compared to the Pt/GCNT and Pt/VXC72 electrodes. For a quantitative comparison of the electrode activity and durability, fitting parameters of the key circuit elements are summarized in Table II.

From Table II, it is clear that the enhanced overall polarization performance of the Pt/GCNT cathode compared to the Pt/VXC72 cathode, as discussed earlier, arises from lower impedances in all three major polarization loss processes, namely ohmic loss ($R_{ohm} + R_{nF}$), charge transfer resistance R_{ct} and mass transfer related impedance Z_O. From the electrode reaction kinetics perspective, the charge transfer resistance present in the Pt/GCNT cathode is smaller than that in the Pt/VXC72 cathode and much smaller than that in the Pt/CNT cathode. In other word, the Pt/GCNT cathode is more catalytically active than the Pt/VXC72 and much more active than the Pt/CNT cathode. In term of electrode durability, an increase in charge transfer resistance of each electrode reflects a decrease in the electrode catalytic activity. The Pt/GCNT cathode shows much smaller relative increases in the charge transfer resistance, and therefore better stability, than the Pt/VXC72 cathode. For example, at 0.6 V, the Pt/GCNT electrode shows a 6.6-fold increase (from 16.4 mΩ to 109 mΩ), whilst the Pt/VXC72 electrode shows a 10.9-fold increase (from 17.5 mΩ to

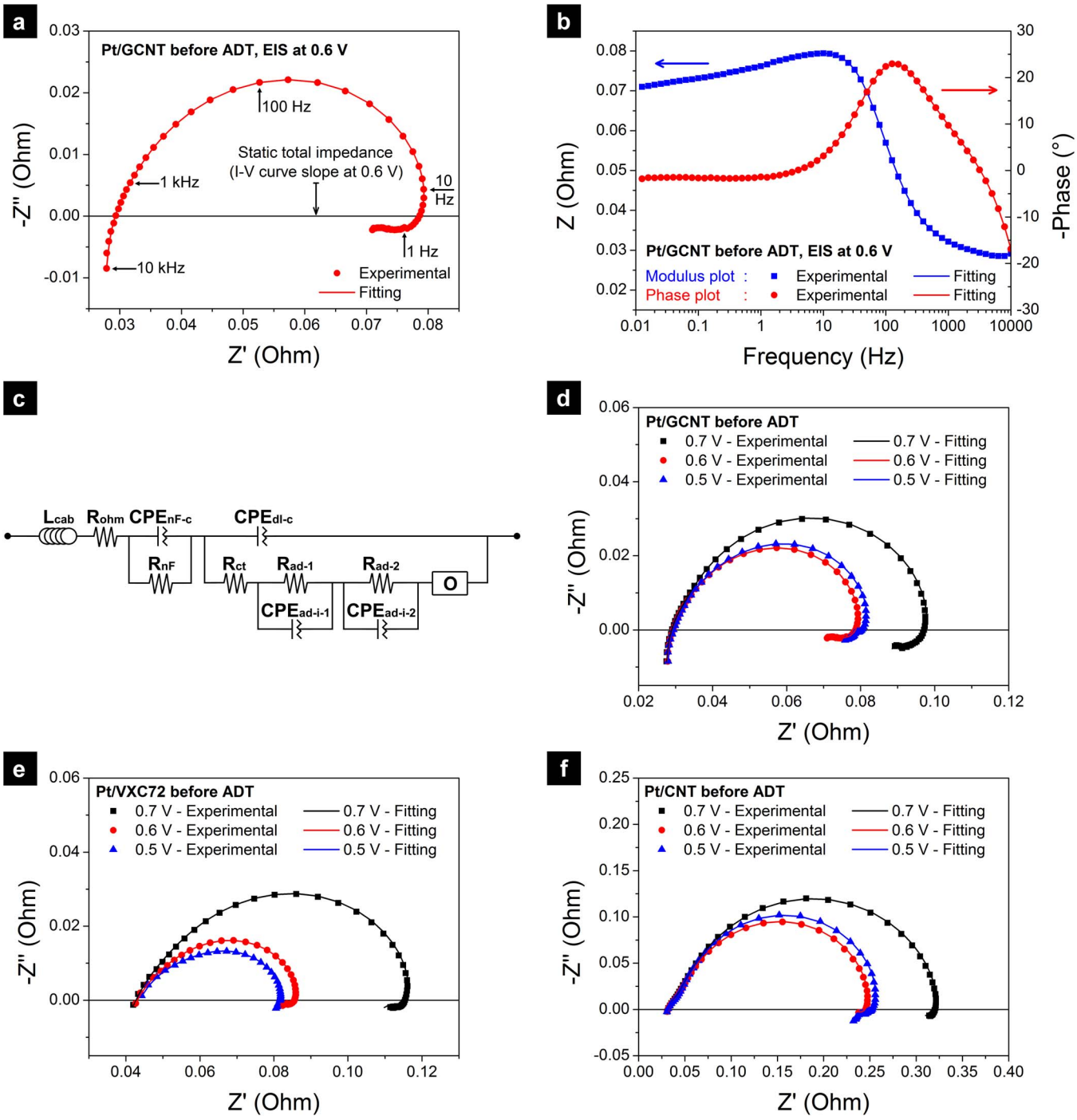

Figure 3. Electrochemical impedance spectroscopy and equivalent circuit fitting of the Pt/GCNT, Pt/VXC72 and Pt/CNT cathodes. The EIS spectrum presented in (a) Nyquist plot and (b) Bode plots of the Pt/GCNT cathode obtained at 0.6 V before the degradation test. (c) equivalent circuit model used for the EIS data fitting. EIS spectra of (d) Pt/GCNT, (e) Pt/VXC72 and (f) Pt/CNT measured at 0.7 V, 0.6 V and 0.5 V, before the degradation test.

Table I. Mathematical expressions of the circuit elements used in the EIS fittings.

Element	Impedance expression	Impedance at limit frequency
L_{cab}	$Z_L = j\omega L$	$Z = 0$ at $\omega = 0$, $Z \to \infty$ at $\omega \to \infty$
R_{ohm}, R_{nF}, R_{ct}, $R_{ad\text{-}1}$ and $R_{ad\text{-}2}$	$Z_R = R$	$Z = R$
$CPE_{nF\text{-}c}$ and $CPE_{dl\text{-}c}$	$Z_{CPE} = \frac{1}{Y_0(j\omega)^n}$ with $0 < n \leq 1$ (capacitive)	$Z = 0$ at $\omega \to \infty$, $Z \to \infty$ at $\omega = 0$
$CPE_{ad\text{-}i\text{-}1}$ and $CPE_{ad\text{-}i\text{-}2}$	$Z_{CPE} = \frac{1}{Y_0(j\omega)^n}$ with $0 > n \geq -1$ (inductive)	$Z = 0$ at $\omega = 0$, $Z \to \infty$ at $\omega \to \infty$
O	$Z_O = \frac{1}{Y_0\sqrt{j\omega}} \tanh(B\sqrt{j\omega})$	$Z = B/Y_0$ at $\omega = 0$, $Z = 0$ at $\omega \to \infty$

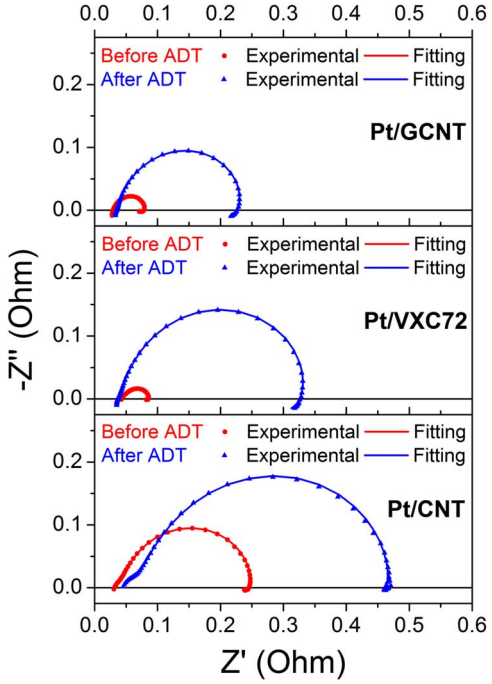

Figure 4. EIS spectra of the Pt/GCNT, Pt/VXC72 and Pt/CNT cathodes measured at 0.6 V, before and after the accelerated degradation test.

190 mΩ) in charge transfer resistance. The Pt/GCNT electrode is both more catalytically active and more electrochemically durable than the Pt/VXC72 electrode.

Pt electrochemical surface area loss and carbon corrosion caused by accelerated degradation test.—In the earlier discussions, the Pt/GCNT cathode shows better electrochemical durability than the Pt/VXC72 cathode. However, the reasons behind the durability enhancement are unclear from the polarization and EIS results. In this section, cyclic voltammetry is used to measure the change in the Pt electrochemical surface area of the cathodes during the accelerated degradation test. Figs. 5a–5c show the cyclic voltammograms of the Pt/GCNT, Pt/VXC72 and Pt/CNT cathodes before ADT and after 10, 20, 50 and 100 cycles of oxidative potential cycling during ADT. The cyclic voltammograms show typical pairs of oxidation-reduction peaks for Pt catalysts, including the hydrogen adsorption-desorption peaks between 0.075 V and 0.35 V vs. RHE and the Pt oxidation-reduction peaks at ≈0.8 V vs. RHE. The active Pt electrochemical surface area present in each electrode is estimated by integrating the adsorption peaks between 0.075 V and 0.35 V vs. RHE in the cathodic scan direction with corrections from the double layer charging background current, as exemplified by the shaded area in Fig. 5a. The adsorption of protons on Pt catalyst surface in the cathodic scan direction proceeds according to:

$$Pt + H^+ + e^- \rightarrow Pt\text{-}H_{ads}$$

By integrating the cyclic voltammograms in the shaded area, the total charge transfer Q_{ads} involving the adsorption of protons is estimated. The active Pt electrochemical surface area is estimated by assuming the charge required to reduce a monolayer of protons on Pt equals 210 μC $cm^{-2}{}_{Pt}$.[33] The gravimetric specific Pt electrochemical surface areas of the Pt/GCNT, Pt/VXC72 and Pt/CNT electrodes throughout the degradation test expressed in absolute surface area and in relative surface area (with respect to the fresh respective electrodes) are shown in Figs. 5d and 5e, respectively. From Fig. 5d, it is clear that all fresh cathodes have similar Pt electrochemical surface areas of between 40 $m^2\ g^{-1}{}_{Pt}$ (Pt/GCNT and Pt/CNT) and 45 $m^2\ g^{-1}{}_{Pt}$ (Pt/VXC72). Whilst the Pt/GCNT cathode has lower Pt electrochemical surface area than the Pt/VXC72 cathode, the Pt/GCNT electrode, as discussed earlier however, has higher catalytic activity than the Pt/VXC72. This suggests that Pt catalysts deposited on GCNT are intrinsically more active than Pt catalysts deposited on carbon black VXC72. Similarly, whilst the Pt/GCNT and Pt/CNT electrodes have nearly identical Pt electrochemical surface areas, the Pt/GCNT cathode is much more active than the Pt/CNT cathode. The Pt catalysts deposited on GCNT are therefore intrinsically much more active than the Pt catalysts deposited on CNT support. This could be supported by the explanation that the high density of graphitic edges present in the GCNT support effectively promotes the reaction kinetics on Pt catalysts, as also suggested by other researchers.[20] The graphitic edges of graphene provide high charge density and reactivity as opposed to the side walls of CNTs.[34] With high density of states present at the graphitic edges, a similar material with high graphitic edge density called graphenated CNTs, as reported by Henry et al., showed strongly enhanced electron transfer kinetics compared to regular CNTs. A two orders of magnitude enhancement in the heterogeneous electron-transfer rate constant was reported in their work.[35] The high charge density and fast electron transfer kinetics provided by graphitic edges may facilitate the charge transfer processes on the GCNT-supported Pt catalyst.

Table II. Equivalent circuit element fitting parameters.

			R_{ohm} mΩ	R_{nF} mΩ	R_{ct} mΩ	$R_{ad\text{-}1}$ mΩ	$R_{ad\text{-}2}$ mΩ	$Z_{O,\,\omega=0}$ (B/Y_0) mΩ
Pt/GCNT	Before ADT	0.7 V	26.0	11.2	29.7	13.9	17.7	3.52
		0.6 V	26.0	11.2	16.4	14.6	8.85	8.27
		0.5 V	26.0	11.2	8.68	5.58	17.8	15.4
	After ADT	0.7 V	26.0	11.2	200	212	125	29.1
		0.6 V	26.0	11.2	109	79.0	18.9	53.6
		0.5 V	26.0	11.2	54.9	94.0	33.3	109
Pt/VXC72	Before ADT	0.7 V	34.5	10.4	32.0	146	29.5	5.14
		0.6 V	34.5	10.4	17.5	22.4	10.5	9.52
		0.5 V	34.5	10.4	10.9	13.1	7.60	17.9
	After ADT	0.7 V	34.5	10.3	365	347	458	30.0
		0.6 V	34.5	10.3	190	132	28.2	48.0
		0.5 V	34.5	10.3	92.0	81.2	37.1	92.2
Pt/CNT	Before ADT	0.7 V	26.0	17.3	173	43.8	68.0	21.1
		0.6 V	26.0	17.3	110	128	26.0	57.0
		0.5 V	26.0	17.3	54.6	31.2	27.2	120
	After ADT	0.7 V	37.0	31.4	645	47.9	15.4	31.2
		0.6 V	37.0	31.4	301	271	15.1	77.8
		0.5 V	37.0	31.4	185	1210	28.7	147

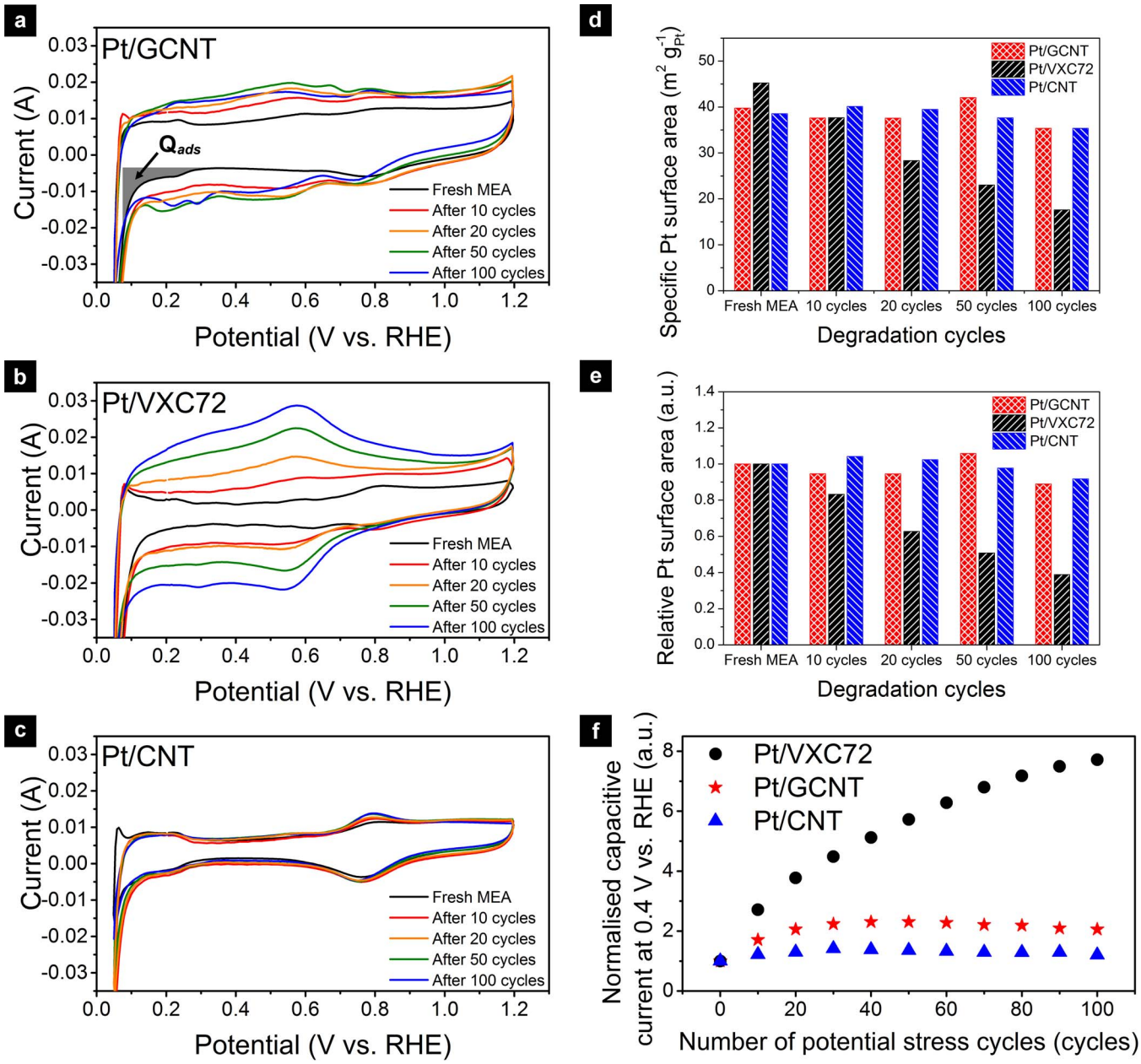

Figure 5. Cyclic voltammetry study of the Pt/GCNT, Pt/VXC72 and Pt/CNT cathodes during the accelerated degradation test. Cyclic voltammograms of the (a) Pt/GCNT, (b) Pt/VXC72 and (c) Pt/CNT cathodes measured before ADT and after 10, 20, 50, 100 cycles of oxidative potential cycling. The degradation of Pt electrochemical surface area of the Pt/GCNT, Pt/VXC72 and Pt/CNT cathodes during ADT, plotted in (d) absolute specific surface area and (e) relative surface area with respect to the fresh electrodes. (f) carbon corrosion of the Pt/GCNT, Pt/VXC72 and Pt/CNT cathodes during ADT, expressed in term of relative changes in double layer capacitance.

In term of catalyst stability, both Pt/GCNT and Pt/CNT cathodes show minimal changes in the Pt electrochemical surface area throughout the degradation test. In contrast, the Pt/VXC72 cathode shows continuous and significant decreases in the Pt electrochemical surface area throughout the degradation test. After 100 cycles of oxidative cycling, the Pt/VXC72 electrode retains a Pt surface area of only 17.6 $m^2\ g^{-1}{}_{Pt}$ (a half of the retained Pt surface area on the Pt/GCNT and Pt/CNT electrodes), as shown in Fig. 5d. The Pt surface area retention of the Pt/VXC72 electrode is only 39% as opposed to ≈90% in the Pt/GCNT and Pt/CNT electrodes, as shown in Fig. 5e. The result confirms the superior stability of the Pt catalysts deposited on crystalline graphitic nanomaterials. We note that, whilst the Pt surface area remains stable in the Pt/GCNT and Pt/CNT electrodes, the electrode catalytic activities do decrease after the degradation test, although at much less degradations compared to the Pt/VXC72 electrode. The activity degradation is probably caused by a restructuring of the Pt nanoparticles to less active crystal surfaces, as suggested by a shift in the hydrogen adsorption-desorption peaks to slightly higher potentials of between ≈0.2–0.3 V vs. RHE, as seen in Figs. 5a–5c. It was demonstrated that the catalytic activity of Pt crystal surfaces decreases in the order Pt (110) > Pt (111) > Pt (100). The corresponding hydrogen adsorption peak potentials of these crystal surfaces shift to higher potentials in the order Pt (110) < Pt (111) < Pt (100).[36]

With the harsh working environment in PEMFCs, such as elevated temperature, high humidity, low pH and high potentials, the carbon support corrosion can be a major cause of the device degradation. The carbon corrosion is evident from the broadening of the CV curves in the double layer charging potentials of 0.4 V – 0.6 V vs. RHE. At a high

potential of 1.4 V used in the degradation test, the carbon oxidation takes place. This results in an increase of the double layer capacitance of the electrode due to the formation of functional groups on the carbon surface and the roughening of the carbon surface.[37,38] The carbon corrosion is therefore evident from the relative changes in the double layer capacitance of the electrode. The cyclic voltammogram of the Pt/GCNT cathode in Fig. 5a shows relatively moderate increases of the double layer capacitance. In contrast, the cyclic voltammogram of the Pt/VXC72 cathode in Fig. 5b shows dramatic increases in the double layer capacitance. This dramatic increase in the double layer capacitance suggests a severe carbon corrosion in the Pt/VXC72 cathode, which may result in the Pt catalyst detachment.[14,15]

To quantitatively compare the increase in the double layer capacitance, and therefore the carbon corrosion, the capacitive current of the cathodes (a half of anodic-cathodic current difference) at the potential of 0.4 V vs. RHE is extracted from the cyclic voltammograms for the fresh cathodes and after every 10 cycles of potential cycling up to 100 cycles. The capacitive current readings are normalized to the respective fresh cathodes and plotted in Fig. 5f. The normalized capacitive currents evolve during ADT differently for the three cathodes. The capacitive current of the Pt/GCNT cathode increases slightly in the first 20 cycles of potential cycling then stabilizes afterwards to 2.1 times the capacitive current of the fresh cathode. This is probably due to the corrosion of any amorphous carbon content present within the first 20 cycles, and the remaining graphitic content is stable afterwards. In contrast, the capacitive current of the Pt/VXC72 cathode continuously increases throughout the 100 cycles of potential cycling and reaches 7.7-fold increase after 100 cycles. The capacitive current of the Pt/VXC72 cathode does not show stabilizing trend within 100 cycles of potential cycling. The results confirm that, compared to the Pt/GCNT catalyst, the Pt/VXC72 catalyst is much more prone to carbon corrosion. This may explain the severe degradation of Pt catalyst activity and the significant loss of Pt electrochemical surface area in the Pt/VXC72 cathode, as discussed earlier. Lastly, the Pt/CNT cathode experiences the least from the carbon corrosion, with the double layer capacitance stabilizes at 1.2 times that of the fresh cathode. Both the GCNT and CNT supports, being highly crystalline graphitic nanomaterials, exhibit superior electrochemical stability to the carbon black support with lower crystallinity.

Electrode structural study with transmission electron microscopy.—As evidenced from the cyclic voltammetry study, the Pt/VXC72 cathode shows a severe degradation after the degradation test, with a ≈60% decrease in the active Pt electrochemical surface area, whilst the Pt/GCNT shows a minimal loss in the Pt surface area. The Pt surface area loss may happen via several processes such as Pt aggregation/coalescence and Pt re-deposition in the Nafion membrane. To investigate these processes, TEM micrographs of the cathode-membrane interfaces are taken for the fresh MEAs and degraded MEAs. Fig. 6 shows the TEM micrographs of the Pt/VXC72 and Pt/GCNT cathodes, before and after the degradation test, at the cathode-Nafion membrane interface.

Fig. 6a shows the cathode-membrane interface region of the Pt/VXC72 cathode before the degradation test. It is observed that the Pt catalyst nanoparticles are well dispersed inside the catalyst layer (bottom-left corner). The Nafion membrane is identified as the homogeneous featureless region at the top-right corner of the micrograph. No Pt catalysts is found in the Nafion membrane. The absence of Pt nanoparticles smearing into the membrane confirms the high quality of the sample preparation method using SEM-FIB dual beam technique. Fig. 6b shows the cathode-membrane interface region of the Pt/VXC72 cathode after the degradation test. The structure of the degraded cathode is highly different from that of the fresh cathode. Firstly, it is clear that the Pt catalyst nanoparticles aggregate densely at the interface between the catalyst layer (bottom-left corner) and the Nafion membrane (top-right corner), in contrast to the well dispersed Pt catalysts in the fresh sample. The dense aggregation of the Pt catalyst after the degradation test may cause a severe decrease of the Pt surface area, consistent with the results from the cyclic voltammetry

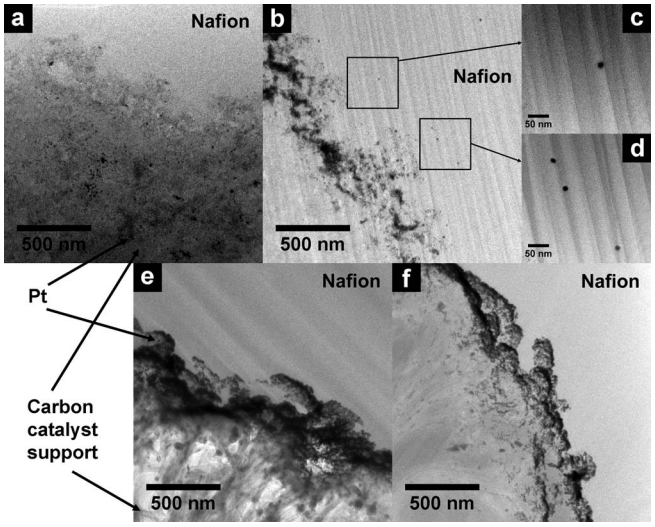

Figure 6. Electrode structural study using transmission electron microscopy. TEM micrographs of the Pt/VXC72 cathode (a) before and (b) after ADT, with (c) and (d) magnified views of the re-deposited Pt nanoparticles inside Nafion membrane. TEM micrographs of the Pt/GCNT cathode (e) before and (f) after ADT.

study. Secondly, Pt nanoparticles are now found inside the Nafion membrane as isolated nanoparticles. Magnified views of selected Pt nanoparticles re-deposited inside the Nafion membrane are shown in Figs. 6c and 6d. The re-deposition of Pt nanoparticles inside Nafion membrane near the cathode was also reported by other studies.[11–13] Both the aggregation of the Pt catalyst at the cathode-membrane interface and the re-deposition of Pt catalyst inside the membrane explain the great loss of Pt catalyst electrochemical surface area in the Pt/VXC72 cathode after the degradation test. The lack of electrochemical stability in the Pt/VXC72 cathode is well demonstrated by the electrode structural study. In contrast, Figs. 6e and 6f show the TEM micrographs of the Pt/GCNT cathode before and after the degradation test, respectively. The degradation behavior of the Pt/GCNT cathode is distinctively different from that of the Pt/VXC72 presented above. Firstly, the location and overall structure of Pt catalyst in the catalyst layer of the Pt/GCNT cathode are very similar in both before and after the degradation test. No significant changes in the electrode structure is observed after the degradation test. The Pt catalyst nanoparticles are located near the cathode-membrane interface, as a characteristic result of the magnetron sputtering catalyst preparation technique used. Secondly, there is no Pt nanoparticles found inside the Nafion membrane after the degradation test. The results suggest the high stability of the Pt/GCNT cathode, consistent with the cyclic voltammetry study where only a minimal change of the Pt electrochemical surface area is detected in the Pt/GCNT electrode after the degradation test.

Summary.—Through a series of electrochemical evaluation methods and transmission electron microscopy technique, it is found that the highly crystalline graphitic nanomaterials, including the GCNT and CNT supports, exhibit much more superior electrochemical stability than the commercial carbon black-supported Pt catalyst. The CNT-supported Pt catalyst, however, possesses a lower catalytic activity than the carbon black-supported Pt catalyst. The lower activity of the Pt/CNT catalyst renders it less competitive to the commercial Pt/VXC72 catalyst. In contrast, the Pt/GCNT catalyst possesses an enhanced intrinsic catalytic activity compared to the Pt/VXC72 catalyst. A combination of both higher catalytic activity and superior electrochemical stability makes the Pt/GCNT much more promising as an advanced catalyst to replace the Pt/VXC72 catalyst.

Conclusions

In this study, we investigate the use of the graphene-carbon nanotube hybrids as the Pt catalyst support in PEMFCs. The Pt/GCNT catalyst exhibits high intrinsic catalytic activity and superior electrochemical stability compared to a commercial carbon black supported Pt catalyst. The enhanced intrinsic catalytic activity of the Pt/GCNT catalyst is attributed to the high density of graphitic edges present in the hybrids. The superior electrochemical stability of the Pt/GCNT catalyst is attributed to the high crystallinity of the GCNT support. The superior stability is expressed by a lower loss in polarization performance, a smaller increase in charge transfer resistance, a lower loss in the platinum electrochemical surface area, a lower rate of carbon corrosion, and a more stable catalyst microstructure. With both high catalytic activity and superior electrochemical stability, the GCNT hybrids demonstrate to be an excellent candidate for an advanced catalyst support in Proton Exchange Membrane Fuel Cells.

Acknowledgments

The authors acknowledge the partial funding support from National University of Singapore (NUS) WBS R284-000-123-112 & R144-000-321-112 and National Research Foundation, Prime Minister's Office, Singapore under its Competitive Research Programme (CRP Award No. NRF-CRP 10-2012-6). K.C.P. acknowledges NUS Graduate School for Integrative Sciences and Engineering for the NGS Scholarship.

References

1. Y. Wang, K. S. Chen, J. Mishler, S. C. Cho, and X. C. Adroher, *Applied Energy*, **88**(4), 981 (2011).
2. S. Sharma and B. G. Pollet, *Journal of Power Sources*, **208**, 96 (2012).
3. V. Mehta and J. S. Cooper, *Journal of Power Sources*, **114**(1), 32 (2003).
4. M. Sahoo, B. P. Vinayan, and S. Ramaprabhu, *RSC Advances*, **4**(50), 26140 (2014).
5. R. Borup, J. Meyers, B. Pivovar, Y. S. Kim, R. Mukundan, N. Garland, D. Myers, M. Wilson, F. Garzon, D. Wood, P. Zelenay, K. More, K. Stroh, T. Zawodzinski, J. Boncella, J. E. McGrath, M. Inaba, K. Miyatake, M. Hori, K. Ota, Z. Ogumi, S. Miyata, A. Nishikata, Z. Siroma, Y. Uchimoto, K. Yasuda, K.-i. Kimijima, and N. Iwashita, *Chemical Reviews*, **107**(10), 3904 (2007).
6. J. Wu, X. Z. Yuan, J. J. Martin, H. Wang, J. Zhang, J. Shen, S. Wu, and W. Merida, *Journal of Power Sources*, **184**(1), 104 (2008).
7. F. A. de Bruijn, V. A. T. Dam, and G. J. M. Janssen, *Fuel Cells*, **8**(1), 3 (2008).
8. S. Zhang, X. Yuan, H. Wang, W. Mérida, H. Zhu, J. Shen, S. Wu, and J. Zhang, *International Journal of Hydrogen Energy*, **34**(1), 388 (2009).
9. P. J. Ferreira, G. J. la O', Y. Shao-Horn, D. Morgan, R. Makharia, S. Kocha, and H. A. Gasteiger, *Journal of The Electrochemical Society*, **152**(11), A2256 (2005).
10. Y. Shao, R. Kou, J. Wang, V. V. Viswanathan, J. H. Kwak, J. Liu, Y. Wang, and Y. Lin, *Journal of Power Sources*, **185**(1), 280 (2008).
11. W. Bi, G. E. Gray, and T. F. Fuller, *Electrochemical and Solid-State Letters*, **10**(5), B101 (2007).
12. K. Yasuda, A. Taniguchi, T. Akita, T. Ioroi, and Z. Siroma, *Physical Chemistry Chemical Physics*, **8**(6), 746 (2006).
13. T. Akita, A. Taniguchi, J. Maekawa, Z. Siroma, K. Tanaka, M. Kohyama, and K. Yasuda, *Journal of Power Sources*, **159**(1), 461 (2006).
14. Z. Tang, H. Y. Ng, J. Lin, A. T. S. Wee, and D. H. C. Chua, *Journal of The Electrochemical Society*, **157**(2), B245 (2010).
15. S. D. Knights, K. M. Colbow, J. St-Pierre, and D. P. Wilkinson, *Journal of Power Sources*, **127**(1–2), 127 (2004).
16. E. Antolini, Carbon supports for low-temperature fuel cell catalysts, *Applied Catalysis B: Environmental*, **88**, 1 (2009).
17. L. M. Roen, C. H. Paik, and T. D. Jarvi, *Electrochemical and Solid-State Letters*, **7**(1), A19 (2004).
18. Z. Tang, C. K. Poh, Z. Tian, J. Lin, H. Y. Ng, and D. H. C. Chua, *Electrochimica Acta*, **56**(11), 4327 (2011).
19. C. Wang, M. Waje, X. Wang, J. M. Tang, R. C. Haddon, and Y. Yan, *Nano letters*, **4**(2), 345 (2004).
20. S. Sharma and B. G. Pollet, *Journal of Power Sources*, **208**(0), 96 (2012).
21. K.-C. Pham, D. H. C. Chua, D. S. McPhail, and A. T. S. Wee, *ECS Electrochemistry Letters*, **3**(6), F37 (2014).
22. A. S. Aricò, A. K. Shukla, H. Kim, S. Park, M. Min, and V. Antonucci, An XPS study on oxidation states of Pt and its alloys with Co and Cr and its relevance to electroreduction of oxygen, *Applied Surface Science*, **172**, 33 (2001).
23. A. Lewera, L. Timperman, A. Roguska, and N. Alonso-Vante, *The Journal of Physical Chemistry C*, **115**(41), 20153 (2011).
24. J. C. Fuggle and N. Mårtensson, *Journal of Electron Spectroscopy and Related Phenomena*, **21**(3), 275 (1980).
25. S. Litster and G. McLean, *Journal of Power Sources*, **130**(1–2), 61 (2004).
26. S.-Y. Huang, P. Ganesan, and B. N. Popov, *Applied Catalysis B: Environmental*, **102**(1–2), 71 (2011).
27. S. Cruz-Manzo, R. Chen, and P. Rama, *Journal of Fuel Cell Science and Technology*, **9**(5), 051002 (2012).
28. O. Antoine, Y. Bultel, and R. Durand, *Journal of Electroanalytical Chemistry*, **499**(1), 85 (2001).
29. S. K. Roy, M. E. Orazem, and B. Tribollet, *Journal of The Electrochemical Society*, **154**(12), B1378 (2007).
30. M. K. Jeon, J. Y. Won, K. S. Oh, K. R. Lee, and S. I. Woo, *Electrochimica Acta*, **53**(2), 447 (2007).
31. Y. Chang, G. Han, M. Li, and F. Gao, *Carbon*, **49**(15), 5158 (2011).
32. S. K. Roy and M. E. Orazem, *Journal of The Electrochemical Society*, **154**(8), B883 (2007).
33. A. A. Franco, *Polymer Electrolyte Fuel Cells: Science, Applications, and Challenges*, p. 616, Pan Stanford (2013).
34. C. B. Parker, A. S. Raut, B. Brown, B. R. Stoner, and J. T. Glass, *Journal of Materials Research*, **27**(07), 1046 (2012).
35. P. A. Henry, A. S. Raut, S. M. Ubnoske, C. B. Parker, and J. T. Glass, *Electrochemistry Communications*, **48**, 103 (2014).
36. V. R. Stamenkovic, B. Fowler, B. S. Mun, G. Wang, P. N. Ross, C. A. Lucas, and N. M. Marković, *Science*, **315**(5811), 493 (2007).
37. C. Li, D. Wang, X. Wang, and J. Liang, *Carbon*, **43**(7), 1557 (2005).
38. E. Negro, R. Latsuzbaia, M. Dieci, I. Boshuizen, and G. J. M. Koper, *Applied Catalysis B: Environmental*, **166–167**, 155 (2015).